Materials Today Nano 22 (2023) 100319

Contents lists available at ScienceDirect

Materials Today Nano

journal homepage: https://www.evise.com/profile/#/MTNANO/login

Synthesis of two-dimensional van der waals superlattices, heterostructures, and alloys from conversion of sequentially layered sub-nanometer metal films

M.J. Motala [a, b, 1], X. Zhang [c, 1], P. Kumar [d, e], E.F. Oliveira [f, g], A. Benton [a, b, h], P. Miesle [a, b, h], R. Rao [a], P.R. Stevenson [a], D. Moore [a, b], A. Alfieri [d], J. Lynch [d], D. Austin [a, b], S. Post [a, b], G. Gao [c], S. Ma [c], H. Zhu [c], Z. Wang [i], I. Petrov [j], E.A. Stach [e], W.J. Kennedy [a], S. Vangala [k], J.M. Tour [c, i], D.S. Galvao [f, g], D. Jariwala [d], C. Muratore [h], M. Snure [k, **], P.M. Ajayan [c, ***], N.R. Glavin [a, *]

[a] Materials and Manufacturing Directorate, Air Force Research Laboratory, Wright-Patterson AFB, OH, 45433, USA
[b] UES Inc., Beavercreek, OH, 45431, USA
[c] Materials Science and Nano Engineering, Rice University, Houston, TX 77005, USA
[d] Electrical and Systems Engineering, University of Pennsylvania, Philadelphia, PA 19104, USA
[e] Materials Science and Engineering, University of Pennsylvania, Philadelphia, PA 19104, USA
[f] Group of Organic Solids and New Materials, Gleb Wataghin Institute of Physics, University of Campinas (UNICAMP), Campinas, SP, Brazil
[g] Center for Computational Engineering & Sciences (CCES), University of Campinas (UNICAMP), Campinas, SP, Brazil
[h] Department of Chemical and Materials Engineering, University of Dayton, Dayton, OH, 45469, USA
[i] Department of Chemistry, Rice University, Houston, TX 77005, USA
[j] Materials Research Laboratory, University of Illinois at Urbana Champaign, Urbana, IL 61801, USA
[k] Sensors Directorate, Air Force Research Laboratory, Wright-Patterson AFB, OH, 45433, USA

ARTICLE INFO

Article history:
Received 2 August 2022
Received in revised form
20 November 2022
Accepted 3 February 2023
Available online 9 February 2023

Keywords:
Transition metal dichalcogenide heterostructures
2D materials
2D superlattices
van der waals materials

ABSTRACT

Manipulation of bulk material properties by controlling layer-by-layer chemistry and structure of nanomaterials has remained an overarching goal of nanoscience and nanoengineering. In the case of two-dimensional (2D) materials, heterostructures consisting of different compositions, stacking, and orientation can serve as a platform for designing bulk material properties; however, fundamental challenges associated with materials processes have limited material quality and impeded scalability. Most attempts to overcome this limitation have relied on slow layer-by-layer growth or meticulous transfer of grown single layers. Our work describes a method to directly convert easily fabricated sub-nanometer metal multilayer heterostructures on both sapphire and SiO_2 substrates followed by conversion to 2D van der Waals superlattices, heterostructures, and alloys. These materials exhibit novel bulk properties compared to individual 2D layers themselves including reduced bandgap, enhanced light-matter coupling, and improved catalytic performance. The process versatility enables tunable orientation, layer structure, and chemistry in an exciting class of 2D nanomaterials and provides an opportunity to generate a wide range of artificially stacked multicompositional 2D structures with controlled morphologies.

Published by Elsevier Ltd.

1. Introduction

Atomic layer-by-layer assembly of two-dimensional (2D) heterostructures has emerged as a versatile platform to realize multifunctional materials by design [1–4]. Over two decades of work has shown that 2D heterostructures generated using layer-by-layer assembly can have properties that are both unique and

* Corresponding author.
** Corresponding author.
*** Corresponding author.
E-mail addresses: michael.snure.1@us.af.mil (M. Snure), ajayan@rice.edu (P.M. Ajayan), nicholas.glavin.1@us.af.mil (N.R. Glavin).
[1] These authors contributed equally to first authorship.

https://doi.org/10.1016/j.mtnano.2023.100319
2588-8420/Published by Elsevier Ltd.

distinct from their individual components. Prominent examples include the observation of superconductivity in twisted graphene [5–7], valley-polarized carrier excitations in transition metal dichalcogenide (TMDC) heterostructures [8], and greater than 90% narrow band absorption in less than 4 nm of excitonic absorber material [9]. The overwhelming majority of these heterostructures are constructed by exfoliation and stacking one material layer at a time, requiring meticulous procedures to achieve the desired structure [10,11]. Direct sequential deposition of TMDC materials have now resulted in routine wafer-scale synthesis of van der Waals (vdW) heterostructures (i.e. a single heterojunction between two dissimilar materials) [12], yet the creation of subsequent layers to form a superlattice or even bulk-like films (i.e. multiple heterostructures in a single stack) has remained much more elusive.

The restriction in achieving 2D superlattices with appreciable thicknesses is predominantly due to the extremely slow nucleation rate of TMDCs on vdW materials. For instance, recent advances in direct synthesis using metal-organic chemical vapor deposition (MOCVD) of 2D superlattices show promise in allowing for large-area monolayer films stacked up to several layers [8]. In this case, however, the first layer must be transferred from the initial growth substrate, and the slow growth rate (monolayer lateral growth rate of ~0.15 nm/min per layer for superlattices) requires over 250 h for seven layers of material. It is paramount that future systems of 2D multilayer superlattice stacks rely on strategies that are performed not just at wafer scale but with feasible processing times in-line with conventional device fabrication and without the requirement of post-growth transfer. In this work, we demonstrate a scalable route toward all-semiconducting 2D TMDC vdW superlattices, heterostructures, and alloys through selenization (or sulfurization) of alternating stacks of sub-nanometer metal films. Uniform deposition of molybdenum (Mo) and tungsten (W) films with thickness as low as 0.7 nm were realized through kinetically controlled magnetron sputtering. The use of metal ion energies approaching 60 eV resulted in continuous, uniform metal films with low surface roughness of below 0.2 nm. The conversion to superlattice structures was accomplished by thermally reacting the wafer-scale ultrathin metal heterostructures in either hydrogen selenide (H_2Se) or hydrogen sulfide (H_2S), leading to the formation of either few-layer TMDC alternating layers or alloys by varying the annealing temperature. The 2D superlattices fabricated in this method reveal a reduced bandgap and improved optical properties relative to the few-layer TMDCs, suggesting use in future optoelectronic device applications. The process is highly scalable, as the processing time for superlattice film fabrication on either sapphire or SiO_2 was approximately 30 min, with a metal growth rate of 0.2 nm/s followed by annealing in a chalcogen hydride (H_2Se or H_2S). At repeating units greater than N = 2 (where N=Mo/W heterostructure), the surface roughening and various kinetic processes result in a transition from horizontally oriented films to vertical orientation, which show promise in catalysis.

2. Experimental methods

2.1. Synthesis

A custom-built magnetron sputtering system was employed for the synthesis of ultrathin metal films (minimum base pressure of 3×10^{-8} Torr) and contained two 1.3" Mac sputter sources (MeiVasc, Inc) held at a distance of 8 cm and a 30° angle from the samples. The metal TMDC precursor layers were deposited utilizing a Pinnacle Plus pulsed power supply (Advanced Energy) utilizing high purity Mo and W targets (Angstrom Sciences, Inc.). The deposition process was optimized to occur at a pressure of 10 Torr under argon with a flow rate of 25 sccm. The pulsed power supplies were operated at 90 W with a pulse frequency of 65 kHz and positive pulse width of 0.4 μ/s.

Following metal deposition, the samples were unloaded and transferred to a vacuum tube furnace for reaction with H_2Se gas. In a typical TMDC conversion, the samples were pumped an hour followed by an additional hour of full pumping under hydrogen gas flow at 200 sccm. The pressure was then increased to 500 Torr and the gas adjusted to 10 sccm hydrogen, 160 sccm nitrogen. A 20 min temperature ramp was used to heat the furnace to desired temperature. After 5 min at equilibrium, the H_2Se was turned on at a flow rate of 150 sccm. This was held for 30 min before the chamber rapidly cooled by opening the tube furnace lid. H_2Se gas was turned off once the temperature was below 400 °C. The tube furnace was only brought to atmospheric pressure after completely cooling. All samples were stored in a glove box to minimize oxidation.

2.2. Raman spectroscopy

Normal and polarized Raman spectra were obtained at room temperature with a Renishaw InVia microscope using a 514.5 nm wavelength excitation laser with ~600 nm spot size (100 × objective lens). The laser power was kept at <1 mW to avoid sample heating. The peak frequencies and widths were obtained by spline baseline subtraction followed by Lorentzian lineshape fitting.

2.3. In-situ transmission electron microscope annealing

In-situ heating of the sample has been carried out using a chip with embedded heaters in close proximity to silicon nitride membranes with a custom holder from Hummingbird Scientific as described in prior studies [13]. Mo and W metal films were deposited with the exact recipe used for sapphire and SiO_2 substrates to form N = 2 metal superlattices. We used bright-field at an accelerating voltage of 200 kV for imaging and selected area electron diffraction. The samples were rapidly heated (>10 C/s) to the desired temperature and then held for approximately 10 min at each temperature before heating to next higher temperature.

2.4. Variable angle spectroscopic ellipsometry

A J.A. Woollam RC2 Ellipsometer was used to characterize the optical properties of $MoSe_2$, WSe_2, and superlattice films. Optical dispersion data were collected from 300 to 2500 nm at 50–80° angles with 5° intervals. A Lorentz multi-oscillator formalism was used for the optical dispersion data analysis using CompleteEASE v6.55. Each respective model incorporated the Si/SiO_2 or single-side polished C-plane sapphire substrate. Model parameters for each film are provided in the Supporting Information (Table S3) and were used to determine n, k, ε1, ε2, and α for the TMDC film responses reported. For simplicity, the derived optical properties from ellipsometry represent an ensemble modeled response (meaning no modeling of individual layers within the respective stacks). However, N = 1 and N = 2 heterostructure films were capable of being modeled in this layer-by-layer fashion yielding overall optical responses commensurate with the non-layer-by-layer modeling approach.

2.5. Theoretical simulations

The density functional theory (DFT) simulations were performed using a projector augmented wave potential in a generalized gradient approximation with the Perdew, Burke, and Ernzerhof exchange-correlation functional [14]. The simulated unit cells of superlattice film were composed of 30 atoms. For the geometry

optimizations, a Monkhorst-Pack k-mesh of 6 × 6 × 1 was used to sample the Brillouin zone and the Kohn–Sham orbitals were expanded in a plane-wave basis set with a kinetic energy cutoff of 60 Ry (~816 eV). The k-mesh was doubled for the electronic structure simulation. The convergence for energy was set to be 10−6 eV between two consecutive steps, and the maximum Hellmann–Feynman forces acting on each atom was set to be less than 0.01 eV/Å upon ionic relaxation. To account for the interlayer interactions, the D3 dispersion corrections were applied for vdW interactions (DFT-D3) [15]. The effects of spin-orbit coupling were considered in all simulations. The dielectric function (ω) was calculated within the random phase approximation (RPA) [16] based on DFT ground-state simulations. All simulations were performed with the computational code Quantum Espresso [17]. It is worth noting that the RPA/DFT simulation with Quantum Espresso is implemented only for norm-conservative pseudopotentials (NC). More details about theoretical simulations can be found in Supporting Information.

2.6. Hydrogen evolution reaction measurements

Hydrogen evolution reaction (HER) experiments were carried out using a CHI708D electrochemical workstation (CH Instruments, Inc.) with a three-electrode configuration. A graphite rod and Hg/Hg_2SO_4 (K_2SO_4, saturated) were used as the counter electrode and the reference electrode, respectively. Typically, a continuous Ar bubble was introduced into 0.5 M H_2SO_4 electrolyte to achieve saturation before the HER test. The linear sweep voltammograms were obtained with a scan rate of 5 mV/s. The Hg/Hg_2SO_4 (K_2SO_4, saturated) reference electrode was calibrated with a reversible hydrogen electrode.

3. Results and discussion

3.1. Wafer-scale conversion of sub-nanometer metal films to TMDCs

Reacting metal thin films with chalcogen vapor at elevated temperatures, as depicted in Fig. 1a, has been an established means of 2D TMDC synthesis [18–20]. For processing at scale (>cm^2) and in few-layer configurations (<5 monolayers), however, 2D materials grown via this method are generally discontinuous and demonstrate non-uniform properties. This restricts the ability to form heterostructures and superlattices as the high interfacial roughness values propagate as film thickness increases. To encourage a transition from 3D island formation to smooth 2D layer-by-layer growth of the metal films, the power applied to the metal target source during sputtering was modulated to adjust the kinetic energy distributions of ionized species. The resultant energy distributions measured for Mo ions is shown in Fig. 1b, depicting a maximum ion energy approaching 60 eV for pulsed DC sputtering and considerably less energy in the DC and high-power impulse magnetron sputtering [21]. The dependence of electrical conductivity on metal film thickness (Fig. 1b, inset) demonstrates that the higher kinetic energy ions in pulsed direct current (DC) power modulation resulted in 2D continuity for the thinnest films, approaching five atomic layers (further details in Supporting Information Figs. S1–4). The ultrathin metal films produced by this technique were amorphous and continuous over large areas, with an atomically smooth surface, as shown by the atomic force microscopy image in Fig. 1c and the optical image (inset, Fig. 1c) of the 1 cm^2 sapphire substrate coated by 0.7 nm Mo. Similar results were confirmed for ultrathin W films. As such, the 0.7 nm metal films were chosen for the remainder of this study as they were the thinnest wafer-scale and continuous metal films demonstrated, but the versatility of the metal synthesis technique can be expanded to both thinner and thicker films. The metal films were then selenized at 500 Torr under a flow of H_2Se (150 sccm), N_2 (160 sccm) and H_2 (10 sccm) over a range of temperatures from 400 to 800 °C (Fig. 1d) to convert to the respective TMDC crystalline structure. Here H_2Se is preferred over Se powder sources due to its low decomposition temperature and simple pyrolysis products [22–24]. The measured Raman spectra and optical constants (i.e. the refractive index, n, and extinction coefficient, k) for monolithic five-layer $MoSe_2$ (Figs. 1e and f) and WSe_2 (Figs. 1g and h) films synthesized using this two-step method reveal properties comparable to films grown via MOCVD. As MOCVD is considered to be the state of the art in scalable 2D TMDC synthesis, the two-step growth methodology described here represents a viable alternative to uniform growth of multilayer 2D materials [25,26].

Sequential sputtering of Mo and W metal sources was employed for the synthesis of metal heterostructure precursor films composed of alternating five layer thick films of Mo and W as shown in Fig. 2a. The presence of alternating metal layers was confirmed by cross-sectional energy dispersive X-ray spectroscopy (EDS). The red and green colored regions in the cross-sectional EDS map in Fig. 2b clearly show discrete horizontal Mo and W layers with little metal film intermixing. For simplicity, we have defined the number of repeating units of Mo/W as N, where N = 2 represents a film composed of Mo/W/Mo/W structure. Following metal deposition, the stacked metal films were selenized for 30 min to ensure full selenization (further information in Fig. S10). The monolithic metal precursor films and superlattice stacks up to N = 8 (Fig. 2c) demonstrate wafer scale uniformity within each film throughout the thickness range in this study. Fig. 2d depicts atomic force microscopy-measured thickness and roughness of selenized metal films after annealing at 600 °C, with insets showing a slight increase in the selenized N = 1 film roughness compared to the metal precursor stack. The roughness values increased significantly beyond N = 2, suggesting a transition from atomic-scale roughness common in horizontally aligned 2D materials (<0.5 nm) for the single TMDC, N = 1 and N = 2 films to nanoscale roughness (>1.0 nm) for films with N ≥ 4. These trends indicate a potential morphology change in the film structure at a certain thickness where a transition occurs after N = 2 and are explored further below. Thickness-dependent Raman spectra from the superlattices annealed at 600 °C (Fig. 2e) exhibit peaks corresponding to both $MoSe_2$ and WSe_2, which are resolved by fitting the spectra to Lorentzian peaks. Peaks from $MoSe_2$ and WSe_2 were observed on both sapphire and SiO_2 substrates (further details in Supporting Information Figs. S16–17) and provide further proof of distinct TMDC layers within the structure. With increasing thickness, the A_{1g} peak frequencies from $MoSe_2$ (WSe_2) blueshift (redshift) in frequency, merging into a single peak at N = 16 (Fig. 2f). These peak shifts suggest increasing strain and alloying with thickness, an effect that has been observed previously in TMDC heterostructures [27]. As mentioned above, one significant advantage of the two-step synthesis technique is the large area uniformity, as indicated by the A_{1g} Raman intensity map of a 2-inch wafer of an N = 2 film and Raman spectra collected from 10 random spots on the film (Figs. 2g and h, respectively).

3.2. Modular orientation and chemistry in vdW heterostructure superlattice films

The 2D vdW structure, orientation, and chemistry was strongly influenced by the conversion temperature from sequentially layered metal films to TMDCs. As the conversion temperature of N = 2 films in the presence of H_2Se vapor increased from 400 °C to 800 °C, increases in grain size were observed in scanning transmission electron microscope cross-sections (Figs. 3a–c). The

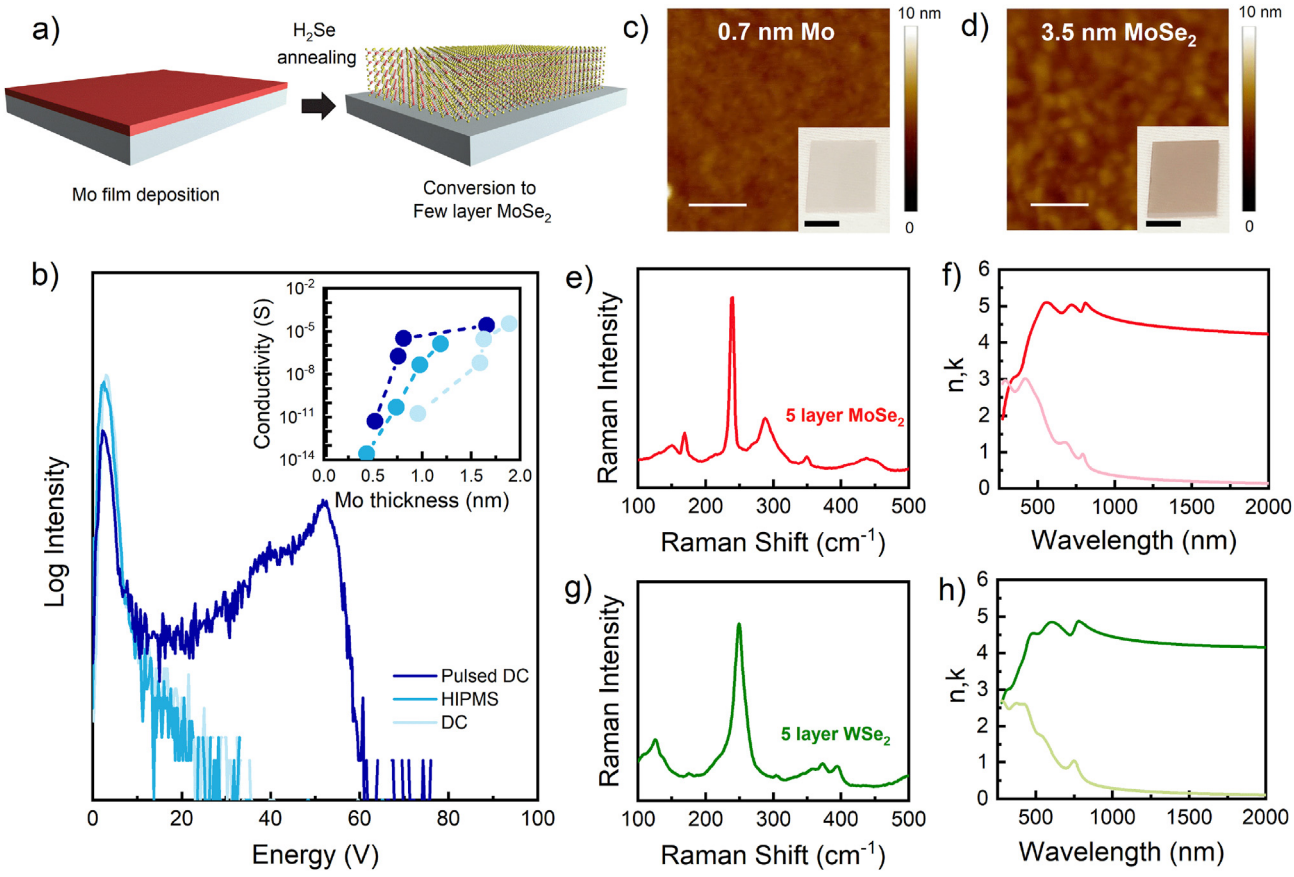

Fig. 1. Two-step synthesis of few-layer TMDCs. (a) Schematic of conversion of Mo or W thin films to subsequent $MoSe_2$ or WSe_2 using H_2Se annealing, (b) Mo^+ Ion energy distribution for various sputtering techniques and inset describes film conductivity as a function of thickness of Mo, (c) AFM height image indicating 0.7 nm Mo film and (d) 3.5 nm $MoSe_2$ film with 50 nm scalebars on AFM image equivalent and inset images of wafers with 0.5 cm scalebars, (e) Raman, and (f) n (darker color) and k (lighter color) values of five layer $MoSe_2$, (g) Raman and (h) n (darker color) and k (lighter color) values of five layer WSe_2. AFM, atomic force microscopy; TMDC, transition metal dichalcogenide.

average grain size improved from 20 nm to 60 nm and from 400 °C to 800 °C and the grain structure migrated from a mixed orientation to a horizontal orientation (further details in Supporting Information Section S4). The improved layer crystallinity at higher temperatures comes as the consequence, however, of a transition from more discrete superlattices to full alloying in N = 2 films at 800 °C, as depicted in the EDS line profiles in Figs. 3a–c. The N = 2 films annealed at 400 and 600 °C showed the Mo/W metal heterostructures were successfully converted to $MoSe_2/WSe_2$ superlattices with atomically sharp interfaces for the 400 °C sample and mostly distinct layering of Mo (W) rich W (Mo) poor regions with an N = 2 repeat for the 600 °C sample. While interfacial mixing is more prevalent in the 600 °C than the 400 °C N = 2 sample, there are some difficulty in determining the exact interface quality due to sample preparation limitations during the transmission electron microscope (TEM) preparation. In the 800 °C annealed films, however, Mo and W concentrations indicated that rather than forming mostly discrete $MoSe_2/WSe_2$ layers, the layered material instead forms a full $Mo_{1-x}W_xSe_2$ alloy. With increasing temperature, the entropic contribution to Gibbs free energy increases favoring mixing and the formation of alloys in TMDCs [28,29]. This establishes a temperature limit for forming mostly TMDC superlattices and resisting much of the metallic intermixing to temperatures at or below 600 °C.

The interplay between conversion temperature and the degree of alloying in the TMDC structure was a result of two competing mechanisms, as the metal films undergo simultaneous thermal annealing and conversion to TMDCs. To investigate the metal crystallization kinetics, an in-situ TEM annealing study was performed using N = 2 films (Mo/W/Mo/W), where the metal films were deposited onto a TEM chip with embedded heaters in close proximity to the silicon nitride membranes (Hummingbird Scientific). Fig. 3d presents bright field TEM images and selected area electron diffraction from the metal films deposited at room temperature and annealed between 400 °C and 600 °C in vacuum (without the presence of H_2Se). As deposited, the metal films remain amorphous up until a temperature between 400 °C and 450 °C, where the first indication of crystallinity is observed. This is evidence by the appearance of distinct Bragg spots, as opposed to diffuse rings observed at lower temperatures. The crystallinity increased with increasing temperature, up to 600 °C. The observed crystallization temperature of >400 °C is consistent with published values of diffusion coefficients for Mo in polycrystalline W [30]. X-ray diffraction spectra of the annealed metal films indicate an improvement in crystallographic order from completely amorphous metal films to metal films with a domain size of 4.5 nm at 600 °C, which strongly contributes to the diffuse interfaces (600 °C) and the alloying (800 °C) as the metals begin to become mobilized in the structure (see further discussion in Supporting Fig. S6).

The competition between the higher temperatures required for highly crystalline materials and lower temperatures for retaining distinct $MoSe_2/WSe_2$ layers resulted in an optimum conversion temperature of 400 °C for retaining chemical separation between the layers, while 600 °C was optimum for retaining some degree of

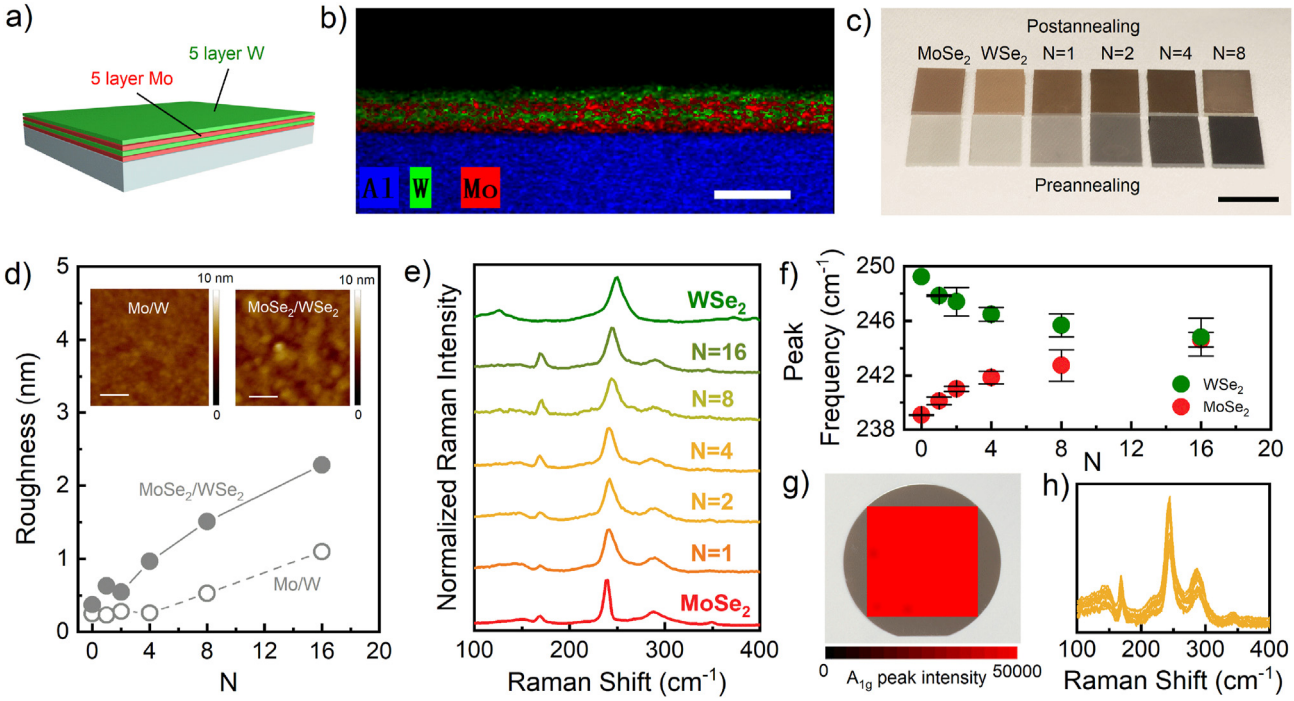

Fig. 2. Synthesis of $MoSe_2/WSe_2$ superlattices. (a) schematic of Mo/W superlattice structure, (b) EDS map of a Mo/W/Mo/W heterostructure with scalebar equivalent to 4 nm, (c) optical image wafer-scale few-layer films and superlattices on sapphire substrates with scalebar equivalent to 1 cm, (d) AFM surface roughness values with inset depicting atomically-flat films and heterostructures with scalebar equivalent to 50 nm, (e) thickness-dependent Raman spectra, (f) Raman peak shift with increasing N value, and (g) Raman map from a 2-inch wafer showing A_{1g} peak intensity, and (h) Raman spectra collected from 10 random spots on the sample indicating highly uniform film properties. AFM, atomic force microscopy; EDS, energy dispersive X-ray spectroscopy.

chemical separation with good crystal quality and horizontal orientation. At 600 °C annealing temperature, the $MoSe_2/WSe_2$ films exhibit AA' stacking (Fig. 3e), consistent with previously reported TMDC superlattice structures [8]. The influence of the conversion process can also be further shown through Raman spectroscopy as a function of temperature shown in Fig. 3f. In this case, the full width at half maximum intensity (FWHM, Γ_{A1g}) of the A_{1g} peak from $MoSe_2$ (20 cm^{-1}) was found to be mostly insensitive to the selenization temperature up to 600 °C and reduces sharply for the film annealed approaching 800 °C (9 cm^{-1}). This decrease in Γ_{A1g} at high temperatures can be attributed to improved crystallinity with annealing temperature, yet the decrease in A_{1g}/E_{2g} intensity ratio (I_{A1g}/I_{E2g}) in polarized Raman suggests films below 600 °C to be less horizontally oriented [31,32]. Strength of the technique developed herein reveals that by simply modulating the conversion temperature, a shift from mixed orientated superlattices to horizontally oriented superlattice with diffuse interfaces to a horizontal alloyed film can all be synthesized directly. Additionally, the formation of MoS_2/WS_2 superlattices was confirmed using similar conditions as that for $MoSe_2/WSe_2$ superlattices (further details are found in Supporting Information Fig. S26).

As the sequentially layered metal films increased to N > 2, there was a profound effect on layer orientation. For N = 8 superlattices, layers became primarily vertically oriented with folding and bending at the top and bottom surfaces (Fig. 3g), consistent with previous reports showing the density of vertically grown layers increased with metal or metal oxide film thickness [33,34]. The constraint on the transition from lateral to vertical orientation at N > 2 is believed to occur due to several factors. First, the atomic-scale morphology of the sequentially layered metal films is controlled by the competition between kinetic and thermodynamic parameters in vapor phase growth processes. Any initial roughness is amplified with continued growth beyond N = 2 as topographical peaks collect material at a higher rate than valleys on the growing film surface due to Ehrlich-Schwoebel and other kinetic barriers [35,36]. As the peaks grow, further shadowing of lower regions from the incident metal flux occurs, amplifying the inequality of growth rates over the entire film surface in a process known as kinetic roughening [37,38]. Surface roughness values from Fig. 2d depict films of N > 2 demonstrating roughness exceeding the thickness of individual layers, resulting in inhomogeneity within each layer from volumes of material isolated by the growth of subsequent metal layers. Second, as the Mo/W superlattice layers selenize the films undergo lattice expansion, which results in a significant amount of strain in thicker films relative to thinner films (further information found in Fig. S18). By reorienting vertically, the strain was relaxed through vertical expansion [33,39]. Finally, the differing diffusion rates of chalcogenide atoms through the vdW interlayer gaps and across the layers can contribute strongly to the thickness-dependent growth orientation [34,39–41].

3.3. Emergent optical and catalytic properties

The wafer-scale superlattice structures represent an enticing platform for designing bulk optical properties through layering of 2D TMDCs of controllable orientation and chemistry. The refractive index n and imaginary part ε_2 of the complex dielectric function of $MoSe_2$, WSe_2, N = 1 heterostructure and N = 2 superlattice, horizontally orientated (HO) alloy (N = 2 annealed at 800 °C), and vertical orientated (VO) alloy (N = 8 annealed at 800 °C) are shown in Fig. 4a and b (additional details in Supporting Information Fig. S30). The spectra of $MoSe_2$ and WSe_2 agree well with previous reports, where two excitonic characteristic peaks are observed at 1.6 eV (A) and 1.8 eV (B) for $MoSe_2$, 1.7 eV (A), and 2.1 eV (B) for WSe_2, respectively, which originate from the spin-split direct gap transitions at the K point of the Brillouin zone [42–44]. It can be

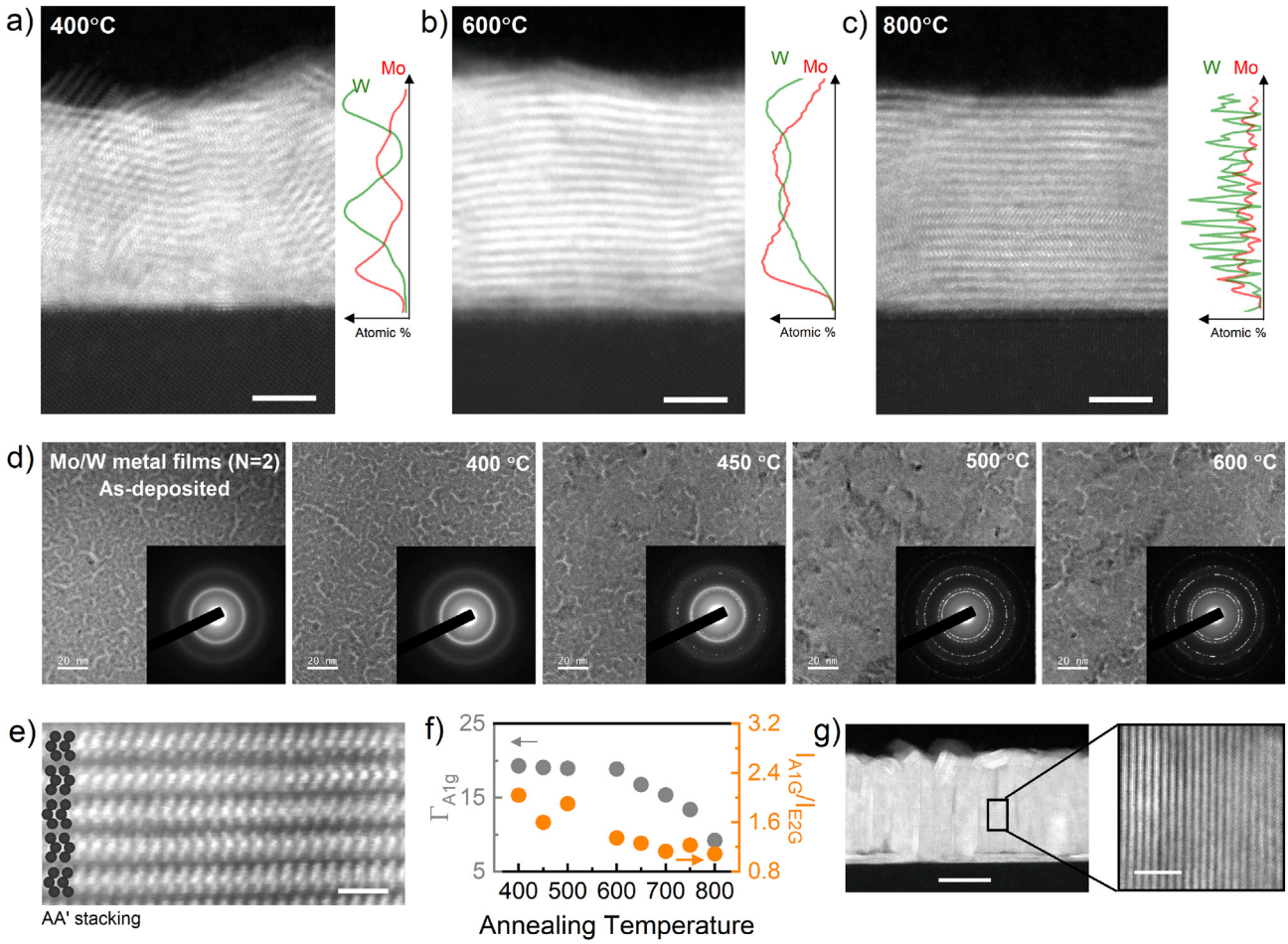

Fig. 3. Temperature and thickness-dependent orientation control in vdW TMDCs. (a) STEM and EDS spectra of N = 2 sample annealed at 400 °C, (b) 600 °C, and (c) 800 °C, with scalebar equivalent to 2 nm, (d) in-situ TEM annealing in vacuum of N = 2 Mo/W metal films without the presence of H_2Se both bright field TEM images and SAED patterns are included, (e) atomically resolved HAADF STEM images showing the 2H-TMDC structure with AA' stacking and scalebar equivalent to 1 nm, (f) Raman A_{1g} FWHM and polarized Raman as a function of annealing temperature, and (g) TEM and atomically resolved STEM images of vertically oriented TMDC alloys with scalebar equivalent to 25 nm and 3 nm, respectively. EDS, energy dispersive X-ray spectroscopy; FWHM, full width at half maximum intensity; HAADF-STEM, high angle annular dark-field scanning transmission electron microscopy; SAED, selected area electron diffraction; TEM, transmission electron microsocpe; TMDC, transition metal dichalcogenide; vdW, van der Waals.

observed that the ε_2 spectra of N = 1 heterostructure and N = 2 superlattice are very similar, except for a slight redshift of N = 2 superlattice relative to N = 1 superlattice heterostructure. Similar trends can be found for the ε_1 and k spectra as well (Supporting Information Fig. S30), which are understandable since the N = 2 superlattice can be considered as a double layer of N = 1 heterostructure and shows a lower bandgap as demonstrated later. Several unique critical points (CPs) were observed in the ε_2 spectra of N = 1 heterostructure and N = 2 superlattice as labeled by A-D in Fig. 4b, which differ in location and relative intensity from the individual $MoSe_2$ and WSe_2 spectra. These CPs located at 1.4 eV (A), 1.7 eV (B), 2.2 eV (C), and 2.6 eV (D) matched well with the values predicted by DFT and RPA displayed in Fig. 4c. The broad FWHM of these experimental CPs can be attributed to multifarious and competitive optical transitions and carrier relaxation channels [45]. These expected transitions have been labeled within the electronic band structure in Fig. 4d (further details in Supporting Information Fig. S29), which are located at the tangent points ($\nabla(E_{CB} - E_{VB}) = 0$) of the curves according to the joint density of states. Similar CPs were observed in the ε_2 spectra of HO alloy film, but the amplitude was lower than N = 1 heterostructure and N = 2 superlattice, indicating that with the same thickness, the optical response of the superlattice film (600 °C) was higher than the alloy film (800 °C). Moreover, the optical properties of the N = 2800 °C alloyed film optical properties closely match films grown via co-sputtering where Mo and W are deposited simultaneously and converted in H_2Se, further highlighting the versatility of the sequentially layered film conversion process to produce high quality alloyed films.

The large ε_2 above 30 and refractive index above 5.7 in the visible spectrum (further details in Supporting Information Fig. S30) for the N = 2 superlattice indicated that the films produced at 600 °C, despite the diffuse interfaces, were excellent candidates for light trapping elements in optoelectronics. This is especially true in comparison to the N = 2 HO alloy films annealed at 800 °C, which show a relatively low ε_2 and refractive index of less than 4 across all wavelengths. Note that diffuse interfaces (or interlayers) play a crucial role in the development of advanced gradient index optical coatings due to the controlled tailoring of process-dependent optical constants. To our knowledge, no such gradient effects have been observed and so well localized to-date for TMDCs. Such diffuse interfaces are expected to offer additional routes toward manipulating excitonic behavior and the resulting optical responses. Furthermore, the highest extinction coefficient k was observed in the N = 2 superlattice samples below 600 nm and was attributed to the significantly enhanced excitonic behavior induced by the quantum confinement effect in the

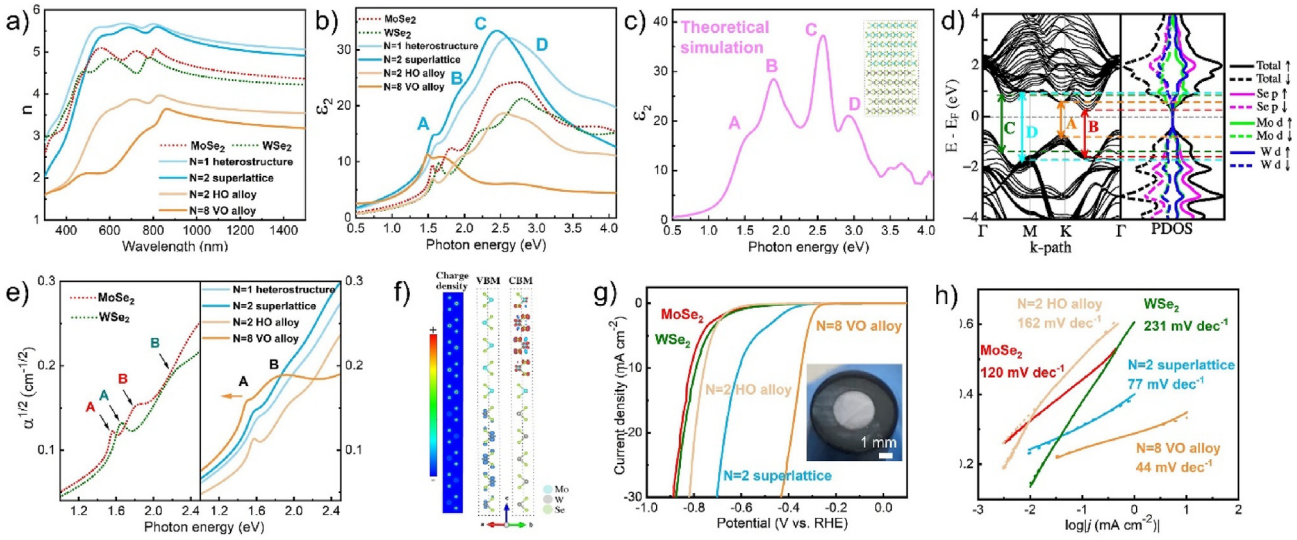

Fig. 4. Optical and catalytic performance of superlattice, heterostructure, and alloyed thin films. (a) The refractive index n and (b) the imaginary part ε_2 of the complex dielectric function of $MoSe_2$, WSe_2, N = 1 and N = 2 superlattice, N = 2 and N = 8 alloy. Critical points A to D is labeled for N = 1 and N = 2 superlattice, (c) theoretically simulated ε_2 spectra of the superlattice with similar critical points A to D. The inset shows the atomic structure of one period of the superlattice, (d) the electronic band structure and the projected density of states of superlattice film, (e) the absorption spectra $\alpha^{1/2}$ of $MoSe_2$, WSe_2, N = 1 heterostructure and N = 2 superlattice, N = 2 horizontal alloy (HO) and N = 8 vertical alloy (VO) with exciton peaks A and B. (f) Charge density and square of the wave function of VBM and CBM for superlattices. (g) Typical cathodic polarization curves and (h) corresponding Tafel plots of $MoSe_2$, WSe_2, N = 2 superlattice, N = 2 HO alloy, N = 8 VO alloy. The inset in (g) shows a picture of transferred film on a 3 mm diameter glassy carbon electrode. CBM, conduction band minimum; VBM, valence band maximum.

superlattice films. In contrast, the CPs of the HO alloy and VO alloy films showed much broader FWHMs and weaker intensities than N = 2 superlattice film but higher absorption near the infrared regime. The permittivity of the N = 2 superlattice lays outside of the generalized Wiener bound for the complex effective medium approximation of $MoSe_2$ and WSe_2 showing that the enhanced permittivity is not an optical phenomena [46]. Instead, the large permittivity is a result of electronic interactions between the $MoSe_2$ and WSe_2. This conclusion is supported by our theoretical study that shows a similarly large ε_2 value in a perfectly stratified superlattice.

The absorption spectra in Fig. 4e depict two expected exciton peaks A and B for both $MoSe_2$ (1.57 eV and 1.82 eV) and WSe_2 (1.66 eV and 2.22 eV) [47,48]. In both the superlattice and alloy films, the A exciton energy decreased with the film thickness, with peak position at 1.59 eV for N = 1 superlattice film, 1.57 eV for N = 2 superlattice and HO alloy films, and 1.49 eV for N = 8 VO alloy film. The redshift in absorption spectra of N = 2 superlattice relative to N = 1 heterostructure agrees with the observations in ε_2 spectra. Additionally, the N = 2 superlattice exhibits slightly higher absorption in the visible and infrared wavelength range compared to N = 1 heterostructure. Using the Tauc plot estimation, the optical bandgap of these films were estimated to be 1.48 eV for $MoSe_2$, 1.53 eV for WSe_2, 1.01 eV for N = 1 heterostructure film, 1.04 eV for N = 2 superlattice film, 1.22 eV HO alloy film, and 1.08 for VO alloy film. The decrease in bandgap in the superlattice films is supported in the simulated electronic band structure and the projected density of states, which predicted that the N = 2 superlattice film has an indirect bandgap of 0.722 eV. This bandgap emerges at the transition from the Γ point to a K point approximately in the middle of the K-Γ path. The simulated electronic bandgap was about 300 meV lower than the optical bandgap extracted from the experimental results, which can be attributed to a common artifact of predicting bandgaps by DFT and the deviation of the Tauc method [49–51]. The square of the wave function of the valence band maximum (Fig. 4f) and the conduction band minimum (further details shown in Support Information Figs. S27–29) suggests that valence band maximum and conduction band minimum are localized in WSe2 layers and MoSe2 layers, respectively, in agreement with the DFT simulations. The electrostatic interactions and the intralayer spin orbit coupling between WSe2 and MoSe2 layers in the superlattice leads to bands splitting and bandgap decreasing [52,53], so that even few-layer WSe2/few-layer MoSe2 structure exhibited a narrower bandgap than monolayer WSe2/monolayer MoSe2. The unique electronic band structure of the superlattices supports the findings that the layer-by-layer assembly of 2D nanomaterials reveals an exciting platform for designing both electronic and optical properties that differ from the properties of the individual layered constituents.

Finally, the ability to control both orientation and chemistry in the superlattice and alloyed structures provided a unique platform for new catalytic properties and applications. To evaluate the HER catalytic activity of $MoSe_2$, WSe_2, $MoSe_2/WSe_2$ N = 2 superlattice, HO alloy and VO alloy, the samples were transferred from the sapphire substrates to glassy carbon electrodes using a PMMA-assisted wet transfer method as shown in Fig. 4e. Typical cathodic polarization curves and corresponding Tafel plots are shown in Figs. 4e and f, respectively, where it was observed that N = 2 superlattice exhibited a better catalytic performance than multilayer $MoSe_2$, WSe_2, and the HO alloy. This was primarily attributed to the narrower band gap in the superlattice (1.04 eV) structure than that of $MoSe_2$ and WSe_2, resulting in more efficient electron transfer as generally observed in catalytic materials [54,55]. Additionally, the VO alloy showed the smallest onset overpotential and Tafel slope among all the films as a result of maximal edge sites on the vertically oriented films. It is worth noting the observed 44 mV/dec Tafel slope of N = 8 alloy film was among the lowest reported Tafel slopes of transition metal diselenide films (further details in Supporting Information Table S5) [53,56–64].

4. Conclusions

The synthesis approach for 2D vdW superlattices, heterostructures, and alloys using conversion of sequentially layered

metal films represents a platform for layer-by-layer design and assembly of 2D semiconductors. The approach herein is highly scalable to large area wafers (2 inch), short processing times (~30 min selenization), reasonable temperatures (400–800 °C), and low cost substrates (SiO_2 or sapphire). By strictly controlling conversion temperature in reactive vapor, a transition from superlattice to alloy and mixed orientation to horizontal orientation was observed for the N = 2 repeating unit. Films annealed at 600 °C depict improved optical light trapping compared to few-layer TMDCs and alloyed films, with both a high absorption and refractive index extending from the visible spectrum into the IR. Above the repeating unit of N = 2, a transition from predominantly horizontally oriented films to vertical orientation was observed which exhibited a low Tafel slope of 44 mV/dec for advanced catalytic performance. As the 2D nanomaterial community is seeking to translate these exciting materials into industrially relevant processes, the synthesis methodology described here represents an intriguing path forward to tune bulk properties of materials through careful layer-by-layer design.

Author contributions

M.M. and X.Z. contributed equally to the first authorship in the manuscript. M.S., P.A., and N.G. contributed equally as corresponding authors in the manuscript. M.M., A.B., C.M. and N.G. developed and characterized the metal deposition process. M.M., S.V., M.S., N.G. performed and optimized the selenization process. M.M., X.Z., P.M., R.R., P.S., A.A., D.M., J.L., D.A., S.P., I.P., S.M., H.Z., Z.W., W.J.K., D.J., M.S., P.A., and N.G. aided in Raman, XPS, structural, SHG, and optical characterization. X.Z., E.O., and D.G. performed the DFT simulations. P.K., G.G., E.S., and D.J. performed TEM imaging studies. Z.W. and J.T. performed catalysis experiments. All authors contributed to drafting the manuscript.

Declaration of competing interest

The authors declare that they have no known competing financial interests or personal relationships that could have appeared to influence the work reported in this paper.

Data availability

Data will be made available on request.

Acknowledgments

N.G. and M.S. acknowledge the support from the Air Force Office of Scientific Research under grant number FA9550-19RYCOR050. EFO and DSG would like to thank the Brazilian agency FAPESP (Grants 2013/08293-7, 2016/18499-0, and 2019/07157-9) for financial support. Computational support from the Center for Computational Engineering and Sciences at Unicamp through the FAPESP/CEPID Grant No. 2013/08293-7 and the Center for Scientific Computing (NCC/GridUNESP) of São Paulo State University (UNESP) is also acknowledged. The work in the laboratory of JMT was funded by the Air Force Office of Scientific Research (FA9550-22-1-0526). H.Z. was supported by the U.S. National Science Foundation (NSF) under award number DMR 2005096. D.J. acknowledges primary support for this work by the Air Force Office of Scientific Research (AFOSR) FA9550-21-1-0035. D. J and A.A. also acknowledge support from the AFOSR under award number FA2386-21-1-4063. D.J. and J.L. also acknowledge support from the AFOSR under award number FA2386-20-1-4074. D.J., E.A.S. and P. K. acknowledge support from National Science Foundation (DMR-1905853) and support from University of Pennsylvania Materials Research Science and Engineering Center (MRSEC) (DMR-1720530) in addition to usage of MRSEC supported facilities. The composition mapping in electron microscopy was carried out at the Singh Center for Nanotechnology at the University of Pennsylvania which is supported by the National Science Foundation (NSF) National Nanotechnology Coordinated Infrastructure Program grant NNCI-1542153.

Appendix A. Supplementary data

Supplementary data to this article can be found online at https://doi.org/10.1016/j.mtnano.2023.100319.

References

[1] K.S. Novoselov, A. Mishchenko, A. Carvalho, A.H. Castro Neto, Science 80 (2016) 353.
[2] A.K. Geim, I. V Grigorieva, Nature 499 (2013) 419–425.
[3] Y. Liu, N.O. Weiss, X. Duan, H.C. Cheng, Y. Huang, X. Duan, Nat. Rev. Mater. 1 (2016), 16042.
[4] Y.K. Ryu, R. Frisenda, A. Castellanos-Gomez, Chem. Commun. 55 (2019) 11498–11510.
[5] Y. Cao, V. Fatemi, S. Fang, K. Watanabe, T. Taniguchi, E. Kaxiras, P. Jarillo-Herrero, Nature 556 (2018) 43–50.
[6] Y. Cao, D. Rodan-Legrain, O. Rubies-Bigorda, J.M. Park, K. Watanabe, T. Taniguchi, P. Jarillo-Herrero, Nature 585 (2020) 215–220.
[7] Y. Cao, V. Fatemi, A. Demir, S. Fang, S.L. Tomarken, J.Y. Luo, J.D. Sanchez-Yamagishi, K. Watanabe, T. Taniguchi, E. Kaxiras, R.C. Ashoori, P. Jarillo-Herrero, Nature 556 (2018) 43–50.
[8] G. Jin, C.-S. Lee, O.F.N. Okello, S.-H. Lee, M.Y. Park, S. Cha, S.-Y. Seo, G. Moon, S.Y. Min, D.-H. Yang, C. Han, H. Ahn, J. Lee, H. Choi, J. Kim, S.-Y. Choi, M.-H. Jo, Nat. Nanotechnol. 16 (2021) 1092–1098.
[9] P. Kumar, J. Lynch, B. Song, H. Ling, F. Barrera, K. Kisslinger, H. Zhang, S.B. Anantharaman, J. Digani, H. Zhu, T.H. Choudhury, C. McAleese, X. Wang, B.R. Conran, O. Whear, M.J. Motala, M. Snure, C. Muratore, J.M. Redwing, N.R. Glavin, E.A. Stach, A.R. Davoyan, D. Jariwala, Nat. Nanotechnol. 17 (2021) 182–189.
[10] S. Masubuchi, E. Watanabe, Y. Seo, S. Okazaki, T. Sasagawa, K. Watanabe, T. Taniguchi, T. Machida, Npj 2D mater, Appl. 4 (2020) 3.
[11] N.R. Glavin, P.M. Ajayan, S. Kar, Adv. Mater. (2022), 2109892.
[12] L. Liu, T. Zhai, Info 3 (2021) 3–21.
[13] P. Kumar, J.P. Horwath, A.C. Foucher, C.C. Price, N. Acero, V.B. Shenoy, E.A. Stach, D. Jariwala, Npj 2D mater, Appl. 4 (2020) 16.
[14] J.P. Perdew, K. Burke, M. Ernzerhof, Phys. Rev. Lett. 77 (1996) 3865–3868.
[15] S. Grimme, J. Antony, S. Ehrlich, H. Krieg, J. Chem. Phys. 132 (2010), 154104.
[16] N.E. Brener, Phys. Rev. B 12 (1975) 1487–1492.
[17] P. Giannozzi, S. Baroni, N. Bonini, M. Calandra, R. Car, C. Cavazzoni, D. Ceresoli, G.L. Chiarotti, M. Cococcioni, I. Dabo, A. Dal Corso, S. de Gironcoli, S. Fabris, G. Fratesi, R. Gebauer, U. Gerstmann, C. Gougoussis, A. Kokalj, M. Lazzeri, L. Martin-Samos, N. Marzari, F. Mauri, R. Mazzarello, S. Paolini, A. Pasquarello, L. Paulatto, C. Sbraccia, S. Scandolo, G. Sclauzero, A.P. Seitsonen, A. Smogunov, P. Umari, R.M. Wentzcovitch, J. Phys. Condens. Matter 21 (2009), 395502.
[18] C.M. Orofeo, S. Suzuki, Y. Sekine, H. Hibino, Appl. Phys. Lett. 105 (2014), 083112.
[19] Y. Zhan, Z. Liu, S. Najmaei, P.M. Ajayan, J. Lou, Small 8 (2012) 966–971.
[20] H. Lin, Q. Zhu, D. Shu, D. Lin, J. Xu, X. Huang, W. Shi, X. Xi, J. Wang, L. Gao, Nat. Mater. 18 (2019) 602–607.
[21] B. Poelsema, R. Kunkel, N. Nagel, A.F. Becker, G. Rosenfeld, L.K. Verheij, G. Comsa, Appl. Phys. A Solids Surfaces 53 (1991) 369–376.
[22] R. Pearson, G. Haugen, Int. J. Hydrogen Energy 6 (1981) 509–519.
[23] X. Zhang, T.H. Choudhury, M. Chubarov, Y. Xiang, B. Jariwala, F. Zhang, N. Alem, G.-C. Wang, J.A. Robinson, J.M. Redwing, Nano Lett. 18 (2018) 1049–1056.
[24] J. Berkowitz, W.A. Chupka, J. Chem. Phys. 45 (1966) 4289–4302.
[25] S.M. Eichfeld, L. Hossain, Y.-C. Lin, A.F. Piasecki, B. Kupp, A.G. Birdwell, R.A. Burke, N. Lu, X. Peng, J. Li, A. Azcatl, S. McDonnell, R.M. Wallace, M.J. Kim, T.S. Mayer, J.M. Redwing, J.A. Robinson, ACS Nano 9 (2015) 2080–2087.
[26] S.M. Eichfeld, C.M. Eichfeld, Y.-C. Lin, L. Hossain, J.A. Robinson, Apl. Mater. 2 (2014), 092508.
[27] M. Zhang, J. Wu, Y. Zhu, D.O. Dumcenco, J. Hong, N. Mao, S. Deng, Y. Chen, Y. Yang, C. Jin, S.H. Chaki, Y.-S. Huang, J. Zhang, L. Xie, ACS Nano 8 (2014) 7130–7137.
[28] K. Bogaert, S. Liu, J. Chesin, D. Titow, S. Gradečak, S. Garaj, Nano Lett. 16 (2016) 5129–5134.
[29] S. Susarla, J.A. Hachtel, X. Yang, A. Kutana, A. Apte, Z. Jin, R. Vajtai, J.C. Idrobo, J. Lou, B.I. Yakobson, C.S. Tiwary, P.M. Ajayan, Adv. Mater. 30 (2018), 1804218.
[30] W. Erley, H. Wagner, Phys. Status Solidi 25 (1974) 463–471.
[31] D. Kong, H. Wang, J.J. Cha, M. Pasta, K.J. Koski, J. Yao, Y. Cui, Nano Lett. 13 (2013) 1341–1347.

[32] M. Hulman, M. Sojková, K. Végsö, N. Mrkyvkova, J. Hagara, P. Hutár, P. Kotrusz, J. Hudec, K. Tokár, E. Majkova, P. Siffalovic, J. Phys. Chem. C 123 (2019) 29468–29475.
[33] S.S. Han, J.H. Kim, C. Noh, J.H. Kim, E. Ji, J. Kwon, S.M. Yu, T.-J. Ko, E. Okogbue, K.H. Oh, H.-S. Chung, Y. Jung, G.-H. Lee, Y. Jung, ACS Appl. Mater. Interfaces 11 (2019) 13598–13607.
[34] Y. Jung, J. Shen, Y. Liu, J.M. Woods, Y. Sun, J.J. Cha, Nano Lett. 14 (2014) 6842–6849.
[35] G. Ehrlich, F.G. Hudda, J. Chem. Phys. 44 (1966) 1039–1049.
[36] R.L. Schwoebel, E.J. Shipsey, J. Appl. Phys. 37 (1966) 3682–3686.
[37] Y.H. Phang, D.E. Savage, R. Kariotis, M.G. Lagally, J. Appl. Phys. 74 (1993) 3181–3188.
[38] T. Salditt, T.H. Metzger, J. Peisl, Phys. Rev. Lett. 73 (1994) 2228–2231.
[39] P. Kumar, B. Viswanath, CrystEngComm 19 (2017) 5068–5078.
[40] E.J.W. Smith, A.H. Piracha, D. Field, J.W. Pomeroy, G.R. Mackenzie, Z. Abdallah, F.C.-P. Massabuau, A.M. Hinz, D.J. Wallis, R.A. Oliver, M. Kuball, P.W. May, Carbon N. Y. 167 (2020) 620–626.
[41] N. Choudhary, H. Chung, J.H. Kim, C. Noh, M.A. Islam, K.H. Oh, K. Coffey, Y. Jung, Y. Jung, Adv. Mater. Interfac. 5 (2018), 1800382.
[42] Y. Li, A. Chernikov, X. Zhang, A. Rigosi, H.M. Hill, A.M. van der Zande, D.A. Chenet, E.-M. Shih, J. Hone, T.F. Heinz, Phys. Rev. B 90 (2014), 205422.
[43] H. Gu, B. Song, M. Fang, Y. Hong, X. Chen, H. Jiang, W. Ren, S. Liu, Nanoscale 11 (2019) 22762–22771.
[44] B.K. Choi, M. Kim, K.-H. Jung, J. Kim, K.-S. Yu, Y.J. Chang, Nanoscale Res. Lett. 12 (2017) 492.
[45] Honggang Gu, Baokun Song, Mingsheng Fang, Yilun Hong, Xiuguo Chen, Hao Jiang, Wencai Ren, Shiyuan Liu, Nanoscale 11 (2019) 22762–22771.
[46] G.W. Milton, Appl. Phys. Lett. 37 (1980) 300–302.
[47] A. Krasnok, S. Lepeshov, A. Alú, S.Z. Butler, S.M. Hollen, L. Cao, Y. Cui, J.A. Gupta, H.R. Gutiérrez, T.F. Heinz, S.S. Hong, J. Huang, A.F. Ismach, E. Johnston-Halperin, M. Kuno, V. V Plashnitsa, R.D. Robinson, R.S. Ruoff, S. Salahuddin, J. Shan, L. Shi, M.G. Spencer, M. Terrones, W. Windl, J.E. Goldberger, G.R. Bhimanapati, Z. Lin, V. Meunier, Y. Jung, J. Cha, S. Das, D. Xiao, Y. Son, M.S. Strano, V.R. Cooper, L. Liang, S.G. Louie, E. Ringe, W. Zhou, S.S. Kim, R.R. Naik, B.G. Sumpter, H. Terrones, F. Xia, Y. Wang, J. Zhu, D. Akinwande, N. Alem, J.A. Schuller, R.E. Schaak, J.A. Robinson, J.R. Schaibley, H. Yu, G. Clark, P. Rivera, J.S. Ross, K.L. Seyler, W. Yao, X. Xu, M. Koperski, M.R. Molas, A. Arora, K. Nogajewski, A.O. Slobodeniuk, C. Faugeras, M. Potemski, C. Zhang, A. Johnson, C.L. Hsu, L.J. Li, C.K. Shih, Rev. Mater. Res 7 (2013), 15972.
[48] H.L. Liu, C.C. Shen, S.H. Su, C.L. Hsu, M.Y. Li, L.J. Li, Appl. Phys. Lett. 105 (2014), 201905.
[49] P. Makuła, M. Pacia, W. Macyk, J. Phys. Chem. Lett. 9 (2018) 6814–6817.
[50] X.D. Zhang, M.L. Guo, W.X. Li, C.L. Liu, J. Appl. Phys. 103 (2008).
[51] N. Sangiorgi, L. Aversa, R. Tatti, R. Verucchi, A. Sanson, Opt. Mater. 64 (2017) 18–25.
[52] X. Fan, D.J. Singh, W. Zheng, J. Phys. Chem. Lett. 7 (2016) 2175–2181.
[53] D.W. Latzke, W. Zhang, A. Suslu, T.-R. Chang, H. Lin, H.-T. Jeng, S. Tongay, J. Wu, A. Bansil, A. Lanzara, Phys. Rev. B 91 (2015), 235202.
[54] A. "Bean" Getsoian, Z. Zhai, A.T. Bell, J. Am. Chem. Soc. 136 (2014) 13684–13697.
[55] Z. Han, R. Gao, Y. Jia, M. Zhang, Z. Lao, B. Chen, Q. Zhang, C. Li, W. Lv, G. Zhou, Mater. Today 57 (2022) 84–120.
[56] I.S. Kwon, I.H. Kwak, T.T. Debela, H.G. Abbas, Y.C. Park, J. Ahn, J. Park, H.S. Kang, ACS Nano 14 (2020) 6295–6304.
[57] L. Najafi, S. Bellani, R. Oropesa-Nuñez, A. Ansaldo, M. Prato, A.E. Del Rio Castillo, F. Bonaccorso, Adv. Energy Mater. 8 (2018) 1–16.
[58] H. Wang, D. Kong, P. Johanes, J.J. Cha, G. Zheng, K. Yan, N. Liu, Y. Cui, Nano Lett. 13 (2013) 3426–3433.
[59] X. Zhou, J. Jiang, T. Ding, J. Zhang, B. Pan, J. Zuo, Q. Yang, Nanoscale 6 (2014) 11046–11051.
[60] F.H. Saadi, A.I. Carim, J.M. Velazquez, J.H. Baricuatro, C.C.L. McCrory, M.P. Soriaga, N.S. Lewis, ACS Catal. 4 (2014) 2866–2873.
[61] D. Gao, B. Xia, C. Zhu, Y. Du, P. Xi, D. Xue, J. Ding, J. Wang, J. Mater. Chem. 6 (2018) 510–515.
[62] X. Ren, Q. Ma, P. Ren, Y. Wang, Int. J. Hydrogen Energy 43 (2018) 15275–15280.
[63] X. Zhou, Y. Liu, H. Ju, B. Pan, J. Zhu, T. Ding, C. Wang, Q. Yang, Chem. Mater. 28 (2016) 1838–1846.
[64] C.H. Mu, H.X. Qi, Y.Q. Song, Z.P. Liu, L.X. Ji, J.G. Deng, Y.B. Liao, F. Scarpa, RSC Adv. 6 (2016) 23–30.